Crystal structure, electronic band structure and high-temperature thermoelectric properties of Te-substituted tetrahedrites Cu12Sb4-xTexS13 (0.5

Yohan Bouyrie, Christophe Candolfi, Viktoriia Ohorodniichuk, Bernard Malaman, Anne Dauscher, Janusz Tobola, Bertrand Lenoir

Crystal Structure, Electronic Band Structure and High-Temperature Thermoelectric Properties of Te-Substituted Tetrahedrites $Cu_{12}Sb_{4-x}Te_xS_{13}$ ($0.5 \leq x \leq 2.0$)

Y. Bouyrie[1,*], C. Candolfi[1], V. Ohorodniichuk[1], B. Malaman[1], A. Dauscher[1], J. Tobola[2], B. Lenoir[1]

[1] *Institut Jean Lamour, UMR 7198 CNRS – Université de Lorraine, Parc de Saurupt, CS 50840, 54011 Nancy, France*

[2] *Faculty of Physics and Applied Computer Science, AGH University of Science and Technology, 30-059 Krakow, Poland*

[*] Contact author: yohan.bouyrie@univ-lorraine.fr

Abstract

Polycrystalline samples of the tetrahedrite phase $Cu_{12}Sb_{4-x}Te_xS_{13}$ with nominal compositions $0.5 \leq x \leq 2.0$ were synthesized by two different synthesis routes: from precursors and from direct melting of the elements. The crystal structure was verified by single-crystal and powder X-ray diffraction (PXRD), both confirming the successful substitution of Te for Sb in both series. Our chemical analyses evidenced differences between the chemical compositions of the two series of samples likely tied to the synthesis method employed and suggesting off-stoichiometry on the Sb site. High-temperature PXRD and differential scanning calorimetry measurements indicate that these materials are stable up to 623 K. Above this temperature, the decomposition process starts and ends up near 748 K where a $Cu_{2-y}S$-type phase is solely observed. In agreement with simple electron counting rule and electronic band structure

calculations, the electrical resistivity and thermopower increase with increasing *x* reflecting the gradual shift from a *p*-type metallic state (*x* = 0.0) to a *p*-type semiconducting behavior (*x* = 2.0). Combined with extremely low lattice thermal conductivity values ($\kappa \approx$ 0.5 W.m^{-1}.K^{-1} at 623 K), this substitution enables to optimize the power factor leading to a maximum thermoelectric figure of merit *ZT* of about 0.8 at 623 K. These results parallel those obtained in prior studies dealing with partial substitutions on the Cu site and enlarge the possibilities to tune the electrical properties of tetrahedrites by extrinsic dopants.

1. Introduction

Thermoelectric generators, which enable direct conversion of heat into electricity, require materials exhibiting an unusual combination of transport properties *i.e.* large thermopower α, low electrical resistivity ρ and low thermal conductivity κ.[1,2] Both amorphous compounds and metals fail in being interesting candidates for the former are good electrical insulators while the latter exhibit low thermopower and large thermal conductivity. Thermoelectric materials should therefore lie on the borders of both types of compounds. These considerations are quantified through the dimensionless figure of merit $ZT = \alpha^2 T / \rho\kappa$ used to evaluate the thermoelectric potential of a material at an operating absolute temperature T.[1,3]

Another level of complexity is related to the fact that all these three transport coefficients are sensitive to the carrier concentration. The best compromise is achieved in semiconductors appropriately doped and adopting a complex crystal structure to minimize the thermal transport. Of the different strategies developed to optimize the *ZT* values, the search for materials that naturally show very low thermal conductivity values have led to the discovery of new classes of materials with high thermoelectric performance. Among others,

this includes Zintl phases, Mo-based cluster compounds, rocksalt-type I-V-VI structures, chalcogenides, cage-like crystal structures such as clathrates, or sulphur-based compounds.[4-18]

Tetrahedrites, a class of natural minerals, belong to this last category of compounds and possess a general chemical formula that may be written within a pure ionic picture as $A_{10}^{+}B_{2}^{2+}X_{4}^{3+}Y_{13}^{2-}$ where *A* is Cu or Ag, *B* is a divalent metal such as Fe, Zn, Ni, Co or Mn, *X* stands for Sb or As and *Y* is S. The nomenclature of these minerals mainly depends on their composition and for some of them, on the location where they were discovered. For instance, Sb-rich compounds are referred to as tetrahedrites while the As-rich analogues are named tennantites. Both families of minerals crystallize with the body-centred-cubic structure described within the space group $I\bar{4}3m$.[19] The unit cell contains 58 atoms distributed over five independent atomic positions (Figure 1). The tetrahedrite structure was first described by Pauling and Neumann as a derivative of the sphalerite structure.[20]

While these compounds have been extensively studied over the last 60 years for mineralogical and geological purposes, little is known on their transport properties. First-principles calculations predicted a metallic ground state for $Cu_{12}Sb_4S_{13}$ with two holes per formula unit.[21] The transport properties are expected to gradually evolve towards a semiconducting state by adding electrons to the structure. Recent studies focusing on the $Cu_{12-x}M_xSb_4S_{13}$ compounds confirmed these expectations and revealed intriguing thermoelectric properties with maximum *ZT* values reaching unity near 700 K for *M* = Zn.[22-28] These high values originate from the combination of intrinsically low lattice thermal conductivity of the order of 0.5 $W.m^{-1}.K^{-1}$ at 300 K and semiconducting-like properties. The poor ability of tetrahedrites to transport heat has been recently shown to originate from the peculiar chemical environment of some of the Cu atoms resulting in strongly anharmonic out-of-plane vibrations of low energy.[29-31] The latter is achieved thanks to the introduction of a divalent cation, which drives the system from a *p*-type metal ($Cu_{12}Sb_4S_{13}$) to a *p*-type semiconductor

(e.g. $Cu_{10}Zn_2Sb_4S_{13}$). Several transition metals successfully substitute for Cu such as Fe, Ni, Mn, Zn or Co, all resulting in semiconducting properties.[21-26,28]

Similar conclusions can be drawn from the study of Lu and Morelli who synthesized $Cu_{12}Sb_{4-x}Te_xS_{13}$ tetrahedrites with x ranging from 0.2 to 1.5 and achieved a maximum ZT of 0.92 at 723 K for x = 1.0.[27] Yet, no detailed investigations of the crystal structure, thermal stability and chemical homogeneity as a function of x was made so far. Herein, in order to provide information regarding these unexplored issues, we extend the study on the $Cu_{12}Sb_{4-x}Te_xS_{13}$ system ($0.5 \leq x \leq 2.0$) by means of transport properties measurements (300 – 700 K), powder and single-crystal X-ray diffraction, differential scanning calorimetry and scanning electron microscopy. First-principles calculations within the Korringa-Kohn-Rostoker method with the coherent potential approximation (KKR-CPA) complement our study. Our experimental findings are compared to those obtained by Lu and Morelli (Ref. 27) and discussed in light of early reports on structural and chemical characterizations of tetrahedrites.

2. Experimental and computational details

Synthesis

Two series of polycrystalline samples of $Cu_{12}Sb_{4-x}Te_xS_{13}$ were synthesized by powder metallurgy using elemental Cu powders (99.99%, ChemPur), S powders (99.999%, StremChemicals), Sb shots (99.999%, 5N Plus) and Te shots (99.999%, 5N Plus) as starting materials. All manipulations were carried out in a dry, argon-filled glove box.

The first series of samples (labeled S1 hereafter) with nominal compositions x = 1.0, 1.25, 1.5, 1.75, 2.0 and 2.5 was prepared from CuS and Sb_2S_3 precursors. Both compounds were synthesized from stoichiometric amounts of elemental powders placed in quartz tubes sealed under secondary vacuum. The ampules were dwelt at 723 K during 48h for CuS and at

843 K during 10h for Sb_2S_3, and finally quenched in room-temperature water. These two compounds together with additional Cu and Te powders were then loaded in stoichiometric amounts into evacuated quartz ampules that were held at 923 K for 12h followed by a final quenching. The resulting ingots were crushed into fine powders, cold-pressed into pellets and further annealed at 723 K for at least 14 days in quartz tubes.

The second series of samples (labeled S2 hereafter) with nominal compositions x = 0.5, 1.0, 1.5 and 1.75 was synthesized by direct reaction of a stoichiometric mixture of the elements sealed under secondary vacuum in quartz ampules. The ampules were then slowly heated up to 923 K at a rate of 0.3 $K.min^{-1}$, dwelt at this temperature for 12 h and then cooled down at a rate of 0.4 $K.min^{-1}$. These slow heating and cooling rates were used due to the low vapor pressure of sulphur, which may result in large pressure in the tubes. The samples were grounded, pelleted and further annealed at 673 K for at least 7 days.

The final products of both series were ground into fine powders and consolidated in graphite dies by spark plasma sintering (SPS) at 723 K under 80 MPa for 10 min. The density of all samples, determined from the weight and the geometric dimensions of the cylindrical ingots, was above 95% and 93 % of its theoretical value for the series S1 and S2, respectively.

Structural characterizations

Powder X-ray diffraction (PXRD) was carried out to assess phase purity with a Bruker D8 Advance diffractometer equipped with a Ge (111) monochromator and using $CuK\alpha_1$ radiation (λ = 1.54056 Å). The lattice parameters were determined from Rietveld refinements of the PXRD data using the Fullprof software.[32]

Structure determination was performed at 300 K on a single-crystal extracted from the as-cast ingot of nominal composition x = 2.0 (series S1). Diffraction data were collected on a Kappa APEX II diffractometer with MoKα radiation (λ = 0.71073 Å) and CCD area

detector. The experimental conditions of data collection and structural refinements performed using the SHELX76 software (Ref. 33) are summarized in Table S1 in the Electronic Supplementary Information file. Note that due to the similar scattering lengths of Sb and Te, the fraction of Te occupying the Sb site could not be refined and was assumed to correspond to the nominal composition *i.e.* $x = 2.0$.

The thermal stability was probed by temperature-dependent PXRD performed on the $x = 1.0$ and 2.0 samples (series S1) between 300 and 800 K under vacuum using a Xpert Pro MPD diffractometer ($CuK\alpha_1$ $\lambda = 1.54056$ Å and $CuK\alpha_2$ $\lambda = 1.54439$ Å, ratio $K\alpha_2/ K\alpha_1 = 0.5$).

Chemical characterizations

The chemical homogeneity and phase purity of the samples were further verified by scanning electron microscope (SEM) using a Quanta FEG (600F, FEI). Images of the surfaces of the samples were collected in the backscattering electron mode (BSE) to contrast the tetrahedrite from impurity phases. Element mapping was performed to assess the spatial distribution of elements in the samples. The chemical compositions were determined on polished surfaces of the consolidated pellets by energy and wavelength dispersive spectroscopy (EDXS/WDXS) with a JEOL J7600F instrument. The chalcopyrite compound $CuFeS_2$ together with ZnS, Sb and Te were used as standards to probe the Cu, S, Sb and Te contents, respectively. Both $CuFeS_2$ and ZnS were chosen due to the similar atomic environments of Cu and S in these structures with respect to those in tetrahedrites allowing the minimization of matrix effects. The actual compositions were obtained from an average of 15 spots measured on the surface of each samples and by normalizing the chemical formulae to 13 sulphur atoms (Table 1). This choice was dictated by the fact that no experimental investigations have reported so far clear evidence of off-stoichiometry on S. This assumption is further corroborated by

refinements of single-crystal XRD data that did not reveal under-stoichiometry on this site. Hereafter, we use the actual Te content to label the samples of both series.

Differential scanning calorimetry (DSC)

DSC measurements were performed on a DSC121 apparatus to further characterize the thermal stability. Powders (~20 mg) were loaded into closed-stainless steel crucibles. The data were collected under an argon flow from 300 K to 873 K with a heating rate of 2 $K.min^{-1}$ to ensure a good thermal equilibrium between the sample and the crucible due to the very low thermal conductivity of these compounds.

Computational details

The electronic band structure of $Cu_{12}Sb_{4-x}Te_xS_{13}$ for $x = 0.0$ and $x = 2.0$ was calculated using the Korringa-Kohn-Rostoker method with the coherent potential approximation (KKR-CPA) that allows to account explicitly for the chemical disorder (*i.e.* treated as random) induced by the partial substitution of Te for Sb.[34,35] The Perdew-Wang formula for the exchange-correlation part was employed in the local density approximation (LDA) formalism to construct the fully-charge self-consistent crystal potentials of the muffin-tin form.[36] The position of the Fermi level was accurately determined by the generalized Lloyd formula. For $x = 2.0$, we used the experimental lattice constants and atomic coordinates determined from our single-crystal refinements. The crystallographic parameters obtained by Pfitzner *et al.*[37] were used for the ternary compound. For well-converged crystal potentials (below 1 mRy) and atomic charges (below $10^{-3}e$), total-, site- and orbital *l*-decomposed densities of states (DOS) were determined using a tetrahedron method for integration in the reciprocal *k*-space.[38] The complex energy dispersion curves were calculated along high-symmetry directions in the first

bcc Brillouin zone. A more detailed discussion on the applied methodology can be found in Refs. 34 and 35.

Transport properties measurement

Electrical resistivity and thermopower were measured simultaneously between 300 and 700 K with a ZEM-3 system (Ulvac-Riko). A careful determination of the high-temperature thermal conductivity (300 – 700 K) was obtained by measuring the thermal diffusivity d by a laser flash technique (LFA 427, Netzsch), the specific heat C_p with a differential scanning calorimeter (Pegasus 403 F3, Netzsch). The thermal conductivity was then calculated from $\kappa = dC_p\alpha_V$ where α_V is the experimental density of the sample. The specific heat was measured on the x = 1.0 and x = 2.0 samples (series S1) while the thermal expansion coefficient β was obtained by the temperature dependence of the lattice parameter inferred from Rietveld refinements of the temperature-dependent PXRD patterns. Herein, β has been assumed to be composition-independent and constant in the temperature range studied. The combined experimental uncertainty in the determination of the *ZT* values is estimated to 17 %.[39]

3. Results and Discussion

Single crystal X-ray diffraction

The trend in the crystal structure upon Te substitution was characterized by X-ray diffraction performed on a single-crystal extracted from the x = 1.79 sample (actual composition) of the series S1. The data were successfully refined within the $I\bar{4}3m$ space group of tetrahedrites (Table S1, Electronic Supplementary Information). The lattice parameter a is larger than that reported by Pfitzner *et al.*[37] for the ternary compound (10.3293(6) Å). A model with a fraction

of Te occupying the S sites was also considered but refinements of the site occupancies led to zero to within experimental accuracy. Thus, we conclude that Te occupies solely the Sb site in these materials.

In the crystal structure, Cu atoms occupy two distinct sites: Cu1 are tetrahedrally coordinated to S1 atoms (Figure 2a) while the Cu2 atoms are in a three-fold planar arrangement to two S1 and one S2 atoms (Figure 2b). S1 atoms show an octahedral coordination with Cu2 atoms (Figure 2c). The S2 atoms are located in tetrahedral sites bonded to one of the Cu2 atoms in threefold coordination, two Cu1 atoms in fourfold coordination and one Sb atom (Figure 2d). Even though all Sb/Te atoms occupy tetrahedral sites, they are only coordinated to three S1 atoms leaving lone-pair electrons on each Sb site (Figure 2e). The relevant crystallographic parameters and the main interatomic distances and bond angles are summarized in Tables S2 and S3 in the Electronic Supplementary Information file. Substituting Te for Sb results in an increase in the Cu2 – Sb/Te and Sb/Te – S1 distances with respect to the parent compound $Cu_{12}Sb_4S_{13}$. Due to the size mismatch between Sb and Te, the Cu2 – Cu2 and Cu2 – S2 distances shrink.

Synthesis and powder X-ray diffraction

The two synthesis methods employed were not equivalent and led to differences in both the annealing time required to obtain phase-pure samples and in the compositional range accessible, especially for nominal compositions below x = 1.0. The direct melting of the elements enabled to achieve phase-pure samples spanning the concentration range between 0.52 and 1.85 as shown in Figure 3a where a representative PXRD pattern and Rietveld refinement obtained on the x = 0.52 sample is presented. Only a very small fraction of impurity phase is revealed by two weak reflections below 30° based on the Bragg positions and the difference between experimental and theoretical patterns. Although this low number

of reflections did not allow an unambiguous identification of the nature of these impurity phases, these peaks may correspond to $CuSbS_2$ and/or Cu_3SbS_4 phases. Impurity phases are no longer visible in other samples in this series and for the samples of the series S1 for $x \geq 1.40$ (Figure 3b). However, the $x = 2.5$ specimen (nominal composition, not shown in Table 1) showed substantial amount of secondary phases suggesting that this value is above the solubility limit of Te in $Cu_{12}Sb_4S_{13}$ while keeping constant the 12 Cu atoms per formula unit. Noteworthy, higher Te contents might be achieved provided the number of additional electrons is counterbalanced by the introduction of vacancies on the Cu sites leading to the hypothetic chemical formula $Cu_{12-y}Sb_2Te_{2+y}S_{13}$. The complete substitution of Te for Sb (*i.e.* $x = 2$ in this formula) would then result in the synthetic goldfieldite $Cu_{10}Te_4S_{13}$, which indeed exists and has recently been studied by inelastic neutron scattering experiments.[29,40] Unlike the above-mentioned samples, the PXRD patterns of the $x = 0.61$ and 0.80 specimen (series S1) still revealed the presence of traces of impurities, observed as additional Bragg peaks, which were indexed to the $Cu_{2-y}S$-type phase.

A compelling experimental evidence of differences between the two series is provided by the variation in the lattice parameters as a function of the Te concentration (Figures 4a and 4b). In the series S2, a increases almost linearly between $x = 0.52$ and 1.85. A similar behavior is observed in the series S1 for compositions $x \geq 1.40$. Yet, below this concentration, the values are significantly higher, reaching 10.4065(2) Å in the $x = 0.61$ sample. Similar values were obtained with several data sets collected on different diffractometers and on powders taken before and after the SPS treatment and hence, are not due to an artifact. Interestingly, these high values trend with those measured on the Cu-rich ternary compound $Cu_{14}Sb_4S_{13}$ and on some polycrystalline $Cu_{12}Sb_4S_{13}$ samples (Figure 4a).[41-44] The latter compound is known to be unstable at room temperature and tends to decompose into Cu-poor

and Cu-rich phases between 403 and 423 K depending on the composition, a mechanism known in mineralogy and geology as an exsolution process.[41-44]

In order to determine whether this mechanism is also at play in the Te-containing tetrahedrites, the response of the crystal structure of the x = 0.61 sample (series S1) upon heating was followed by PXRD from 300 K to 483 K with steps of 30 K. The results, shown in Figure 4c, do not evidence any exsolution process, the lattice parameter smoothly increasing with temperature up to 483 K due to the thermal expansion of the unit cell. This phenomenon is reversible as shown by the data collected upon cooling to room temperature. This result is in agreement with the absence of clear evidence of a separation or broadening of the diffraction peaks. However, the possibility that Te-poor samples exsolve below room temperature cannot be excluded. Between 498 and 623 K, a shows a steeper rise in temperature which might correspond to the decomposition threshold. Unlike this sample, the lattice parameter of the x = 1.79 specimen increases quasi-linearly in the whole temperature range.

Chemical homogeneity and actual compositions

BSE and elemental mapping images show that Te is homogeneously distributed within the tetrahedrite phase regardless of the Te content (Figures S1, S2 and S3, Electronic Supplementary Information). However, these experiments indicated the presence of impurity traces determined to be $Cu_{2-y}S$ and/or elemental Te depending on the nominal composition. The chemical compositions measured by EDXS/WDXS experiments, and listed in Table 1, reveal a very good correlation between the nominal and actual compositions for the series S2 in the whole concentration range investigated. Nevertheless, these analyses seem to indicate excess Cu in all samples except for x = 1.85. This trend holds true for the series S1 where a systematic deviations from 12 Cu atoms per formula unit is observed for $x \leq 1.40$. Yet, both

the $x = 0.61$ and $x = 0.80$ samples of this series also show significant deviations on the Sb site, the sum of the Sb and Te concentrations largely exceeding the expected stoichiometry of 4 atoms per formula unit. Sb-rich compositions have already been reported in the $Cu_{12}Sb_4S_{13}$ tetrahedrite,[41-44] and, interestingly, this excess expands the unit cell volume with lattice parameter above 10.40 Å, as observed in the present samples. These results are thus consistent with our PXRD analyses and show that deviations from stoichiometry can be also achieved in quaternary tetrahedrites. Of note, these findings are in agreement with the general fact that synthetic tetrahedrites can show significant variations in the predicted 12-4-13 stoichiometry while natural tetrahedrites appear more stoichiometric in spite of the large number of elements present in their composition.[45] We note that it remains unclear which experimental parameter is responsible for these deviations in the first series of samples. The possibility that slight off-stoichiometry exists in the composition of the precursors cannot be strictly ruled out. In any case, it would be interesting to determine whether these deviations can be controlled within the second synthesis route *i.e.* starting from off-stoichiometric nominal compositions.

Thermal behavior

PXRD patterns were measured every 50 K between 623 and 823 K on the $x = 0.61$ and $x = 1.79$ samples (series S1) to probe the thermal stability (Figure S4 and S5, Electronic Supplementary Information). Room-temperature data collected under similar experimental conditions are also added for comparison purposes. For both samples, no sign of secondary phases is observed up to 623 K, while above this temperature first additional reflections become visible. These peaks were identified as the cubic $CuSbS_2$ compound and indicate that thermal decomposition starts already between 623 and 673 K. Further increasing the temperature leads to a substantial increase in the peak intensity of $CuSbS_2$ up to 723 K. Eventually, the tetrahedrite structure has completely disappeared at 733 K leaving a $Cu_{2-y}S$-

type phase only visible. The thermal decomposition process of the x = 0.61 sample is somewhat different. The first additional Bragg peaks correspond to a $Cu_{2-y}S$-type phase. The tetrahedrite structure is then fully decomposed when the temperature rises to 748 K. This decomposition process is consistent with that reported by Skinner and Makovicky for the ternary compound $Cu_{12}Sb_4S_{13}$ which decomposes into $CuSbS_2$ and $Cu_{2-y}S$ at 816 K and by Barbier *et al*. on the same composition (with a temperature onset at 791 K).[28,41,42]

In agreement with these findings, the x = 1.79 sample shows signs of endothermal peaks at 615 and 680 K and a clear decomposition event at 720 K according to our DSC analyses (Figure 5a). For the x = 0.61 sample, no clear event is observed below 740 K except for a change of slope near 610 K (Figure 5b) which might correspond to the onset of thermal decomposition. For comparison, the data collected on the x = 1.01 sample of the second series is shown in Figure 5c. Below the decomposition threshold at 840 K, only one weak exothermic peak can be distinguished at 610 K whose origin remains unclear.

Although the decomposition process observed in Te-substituted tetrahedrites is consistent with prior studies, the temperatures at which this process sets in are clearly lower than those observed in the parent compound $Cu_{12}Sb_4S_{13}$ suggesting that substituting Te for Sb does not enhance the thermal stability in the present case.[28,41,42] This behavior contrasts with experimental results obtained in $Cu_{10.4}Ni_{1.6}Sb_4S_{13}$ where the substitution of Ni for Cu led to an increase in the thermal stability to 861 K.[28]

Taken together, these experiments suggest that these tetrahedrites are thermally stable up to around 600 K. To qualify these materials as candidates for mid-range-temperature thermoelectric applications would nevertheless require additional thermogravimetric measurements to determine the weight loss over several hours between 500 and 700 K. Indeed, Barbier *et al*.[28] showed that sulphur volatilization is likely the main mechanism leading to a substantial weight loss at 723 K.

Electronic band structure calculations

The electronic band structures of the $Cu_{12}Sb_{4-x}Te_xS_{13}$ compounds are shown in Figure 6. Here, we restrict our analysis to the top of the valence bands and their evolution with x. The calculated dispersion relations $E(k)$ of $Cu_{12}Sb_4S_{13}$ are in agreement with the results of Lu *et al.*[21] The main characteristics are an indirect energy gap of ~1.4 eV and weakly-dispersive valence bands along the Γ – H, N – H and N – P directions. These nonparabolic bands may result in high effective masses of holes. Centered at the Γ point, the valence band edge consists of two asymmetric bands as well as a lower band with a maximum at – 0.11 eV. The Fermi level lies inside the valence bands, confirming the *p*-type metallic character of this compound. Our results also further show that two unoccupied states per formula unit should be filled to achieve semiconducting behavior *i.e.* for x = 2.0. Interestingly, in the x = 2.0 compound, our KKR-CPA calculations result in an energy gap lower than that obtained by Lu. *et al.*[21] for $Cu_{12}Sb_4S_{13}$. We can also observe that the shape of the valence band edge is modified with varying the Sb/Te ratio. Yet, this effect seems to be related to an evolution of the interatomic distances in the series $Cu_{12}Sb_{4-x}Te_xS_{13}$ with x rather than with the Sb/Te disorder itself.

Because the shape of the valence bands near E_F governs the transport properties of these materials, it is essential to gain a deeper understanding of the nature of the states forming these bands. Regardless of the Te concentration, the DOS near E_F is dominated by Cu1 states together with a nearly equal contribution from the S1 and Cu2 states (Figure 7). The flat bands near E_F give rise to a strongly varying DOS likely at the origin of the large thermopower values reported in tetrahedrites. Noteworthy is the difference in the degree of overlapping of the Sb and Te *p*-states (*i.e.* the disorder site). While the valence edge states exhibit a strong bonding character, the conduction-band states lying just above the gap (see Figure 7) show a non-bonding behavior. This fact reflects the larger spatial extension of the *p*-

Te states with respect to the *p*-Sb states and is consistent with the solubility limit of Te in $Cu_{12}Sb_{4-x}Te_xS_{13}$ that prevents from reaching compositions with $x > 2.0$.

Transport properties

The temperature dependence of the electrical resistivity for both series of samples is shown in Figures 8a and 8b. The ρ values of the series S2 are lower than those of the first series for similar substituting levels. The overall variation in $\rho(T)$ with increasing x is similar in both series of samples and in agreement with our first-principles calculations predicting a progressive filling of the valence states. As expected from simple chemical counting rules, a semiconducting behavior typified by an activated-like temperature dependence is observed at the highest Te contents (x = 1.81 and 1.85 for the series S1 and S2, respectively). However, this picture remains too simple to explain the trends observed in the entire x range. This is seen in the semiconducting character retained at lower Te contents in the series S1 that might hint at deviations of the Te valence state from the predicted +4 state. In principle, Hall effect data may help shed light on this issue by probing the hole concentration as a function of x. Yet, as Lu *et al.*[21], our attempts to realize these experiments remained so far unsuccessful due to quasi-null Hall voltage. The x-dependence of the thermopower faithfully reflects the $\rho(T)$ data (Figures 9a and 9b). The decrease in ρ is accompanied by an increase in the magnitude of α which varies at 300 K between 135 and 200 $\mu V.K^{-1}$ and 95 and 190 $\mu V.K^{-1}$ for the S1 and S2 series, respectively. Regardless of the composition and the series, α monotonically increases with temperature up to 673 K. Thus, the influence of Te on the electronic properties appears similar to that of transition metals reported in other quaternary tetrahedrites.[21-28]

The temperature dependence of the specific heat was measured on the x = 0.80 and x = 1.79 samples (Figure S6, Electronic Supplementary Information). In both cases, and in agreement with the measurements carried out by Lu *et al.*[21], the C_p values are close to the

Dulong-Petit limit given by $3NR$ where N is the number of atoms per formula unit and R is the gas constant (*i.e.* 0.43 J.g^{-1}.K^{-1} for $Cu_{12}Sb_4S_{13}$). While the C_p data of the x = 1.81 sample are nearly temperature-independent, a slight but noticeable increase with T is observed in the x = 0.81 sample for which C_p reaches 0.45 J.g^{-1}.K^{-1} at 675 K. These different behaviors are likely due to an additional electronic contribution in the latter sample, which is expected to increase linearly with temperature as long as the charge carriers remain degenerate.

Figures 10a and 10b present the temperature dependence of the thermal conductivity for the series S1 and S2, respectively. For the series S1, κ exhibits very low values ranging between 0.45 and 0.60 W.m^{-1}.K^{-1}, in agreement with prior studies. We note that even lower κ values have been recently measured by Heo *et al.*[25] in several tetrahedrites $Cu_{10}M_2Sb_4S_{13}$ (M = Cu, Zn, Ni, Mn, Co and Fe). Yet, their values are lower by a factor of two at 300 K than those measured by Suekuni *et al.*[24] on the same compositions. The reason of this discrepancy remains unclear and further work is required to determine whether such extremely low values are indeed achievable in tetrahedrites. The more pronounced metallic character of the samples of the series S2 results in higher κ values that vary at 300 K from 0.45 up to 1.1 W.m^{-1}.K^{-1} in the x = 1.85 and 0.52 samples, respectively. In both series, the tendency of κ to decrease with increasing Te content trends well with higher electrical resistivities in more Te-containing samples.

The total thermal conductivity is the sum of lattice (κ_L) and electronic (κ_e) contributions that can be separated using the Wiedemann-Franz relation $\kappa_e = LT/\rho$ where L is the Lorenz number. In principle, L depends on temperature via the carrier concentration and its scattering mechanisms. Their knowledge enables estimating L within a single-parabolic band model, which describes well transport in various thermoelectric compounds. Because of the lack of information on these properties, we estimated κ_e by assuming a constant L value of 1.8×10^{-8} V^2.K^{-2} *i.e.* a value derived recently in $Cu_{10.5}Ni_{1.5-x}Zn_xSb_4S_{13}$

tetrahedrites by Lu *et al.*[46] As depicted in Figure 10c, κ_L is very low in the entire range of compositions and comparable to that measured in complex Zintl phases or Mo-based cluster compounds such as $Yb_{14}MnSb_{11}$, $Yb_9Mn_{4.2}Sb_9$ or $Ag_xMo_9Se_{11}$ ($3.4 \leq x \leq 3.8$) for instance.[4-9] It is instructive to compare κ_L to the glassy limit of the thermal conductivity κ_m calculated from[47]

$$\kappa_m(T) = \left(\frac{\pi}{6}\right)^{\frac{1}{3}} k_B V^{-\frac{2}{3}} \sum_i v_i \left(\frac{T}{\theta_i}\right)^2 \int_0^{\theta_i/T} \frac{x^3 e^x}{(e^x - 1)^2} dx \qquad (1)$$

In Eq.(1), the sum is performed over one longitudinal and two transverse modes, V is the average volume per atom, $\theta_i = v_i(\hbar / k_B)(6\pi^2 / V)^{1/3}$ and v_i are the Debye temperatures and the sound velocities, respectively, associated to the longitudinal and transverse modes. An estimate of the transverse v_T and longitudinal v_L sound velocities of the $Cu_{12}Sb_{4-x}Te_xS_{13}$ compounds was obtained using the experimental elastic moduli measured by resonant ultrasound spectroscopy by Lu and Morelli on synthetic $Cu_{12}Sb_4S_{13}$ and on several composite materials $(Cu_{12}Sb_4S_{13})_y(Cu_{9.7}Zn_{1.9}Fe_{0.4}As_4S_{13})_{1-y}$ with $0 \leq y \leq 1$.[48] Using the values of both the shear G and bulk B moduli, v_T and v_L can be determined from the relations $G = \alpha_V v_T^2$ and $B = \alpha_V (v_L^2 - \frac{4}{3} v_T^2)$. Depending on the fraction y, these elastic moduli were found to vary significantly between 12.5 and 25 GPa (y = 1) and 35 and 60 GPa (y = 0) for G and B, respectively. Even though the differences are rather large, we considered the lower limit to estimate the sound velocities and the related properties described below. This choice is justified by the present compositions, which are closer to the y = 1 composition, and by the fact that using the upper limit leads to κ_m values significantly higher than the experimental ones. This approach yields v_T = 1577 m.s^{-1} and v_L = 3218 m.s^{-1} in good agreement with that

derived in the above-mentioned composites and with that obtained in a single-crystalline natural specimen by inelastic neutron scattering.[29,48] As shown in Figure 10c, κ_L nears κ_m above 300 K (~ 0.5 $W.m^{-1}.K^{-1}$ at 300 K) suggesting that the scattering length of phonons is close to its minimum value *i.e.* $\lambda/2$ for a phonon of wavelength λ.

The temperature dependence of the *ZT* values of $Cu_{12}Sb_{4-x}Te_xS_{13}$ is shown in Figures 11a and 11b. A maximum *ZT* of ~ 0.8 at 623 K is reached in the $x = 0.61$ and 0.80 samples of the first series in agreement with the results of Lu and Morelli and with prior studies on substitutions on the Cu site.[21-28] Slightly lower values are achieved in the samples of the second series with maximum values of ~ 0.65 at 623 K measured in the $x = 0.52$, 1.01 and 1.41 samples.

4. Conclusion

By a combined structural, chemical and transport properties study, we have demonstrated the possibility to tune the thermoelectric properties of the tetrahedrites $Cu_{12}Sb_4S_{13}$ upon substituting Te for Sb. The two synthesis routes used to prepare these samples resulted in differences in the crystal structure and chemical composition of the samples suggesting that off-stoichiometry can be achieved in quaternary tetrahedrites. DSC and high-temperature PXRD measurements revealed that these materials remain stable up to 623 K. In agreement with first-principles calculations, varying the Te content allows for a fine control of the transport properties, which gradually evolve from metallic to semiconducting with increasing the Te content. The extremely low thermal conductivity is close to the minimum theoretical value and is the key factor that gives rise to a maximum *ZT* value of about 0.8 at 623 K for $x = 0.61$ and $x = 0.80$. Despite differences between the chemical compositions of both series, the overall *ZT* values were found to be similar to within experimental uncertainty suggesting little influence of off-stoichiometry at high temperatures. Because substitutions on both the

Cu and Sb sites significantly improve the thermoelectric performance of tetrahedrites, double substitutions on these two sites may be an interesting way to further optimize the *ZT* values in this family.

Acknowledgements

The authors thank P. Villéger and G. Medjahdi for the high-temperature PXRD measurements and S. Mathieu for the EDS/WDS analyses.

Electronic supplementary information (ESI) available: Tables S1 and S2 presenting the relevant crystallographic parameters, the main interatomic distances and bond angles of the single crystal; BSE images and X-ray mapping on the x = 0.61, 1.40 and 1.79 samples (series S1); High-temperature PXRD patterns of the x = 0.61 and 1.79 samples (series S1); Temperature dependence of the specific heat of the x = 0.80 and 1.79 samples (series S1).

References

1. *Thermoelectrics and its Energy Harvesting,* edited by D. M. Rowe (CRC Press, 2012).
2. G. J. Snyder and E. S. Toberer, *Nature Mater.*, 2010, **7**, 105.
3. H. J. Goldsmid in *Thermoelectric Refrigeration* (Temple Press Books, Ltd.: London, 1964).
4. S. R. Brown, S. M. Kauzlarich, F. Gascoin and G. J. Snyder, *Chem. Mater.*, 2006, **18**, 1873.
5. S. K. Bux, A. Zevalkink, O. Janka, D. Uhl, S. Kauzlarich, J. G. Snyder and J.-P Fleurial, *J. Mater. Chem. A*, 2014, **2**, 215.
6. U. Aydemir, A. Zevalkink, A. Ormeci, Z. M. Gibbs, S. Bux and G. J. Snyder, *Chem. Mater.*, 2015, **27**, 1622.
7. P. Gougeon, P. Gall, R. Al Rahal Al Orabi, B. Fontaine, R. Gautier, M. Potel, T. Zhou, B. Lenoir, M. Colin, C. Candolfi and A. Dauscher, *Chem. Mater.*, 2012, **24**, 2899.
8. R. Al Rahal Al Orabi, P. Gougeon, P. Gall, B. Fontaine, R. Gautier, M. Colin, C. Candolfi, A. Dauscher, J. Hejtmanek, B. Malaman and B. Lenoir, *Inorg. Chem.*, 2014, **53**, 11699.
9. T. Zhou, B. Lenoir, M. Colin, A. Dauscher, R. Al Rahal Al Orabi, P. Gougeon, M. Potel and E. Guilmeau, *Appl. Phys. Lett.*, **98**, 162106 (2011).
10. M. D. Nielsen, V. Ozolins and J. P. Heremans, *Energy Environ. Sci.*, 2013, **6**, 570.
11. H. Liu, X. Shi, F. Xu, L. Zhang, W. Zhang, L. Chen, Q. Li, C. Uher, T. Day and G. J. Snyder, *Nature Mater.*, 2012, **11**, 422.

12. Y. He, T. Day, T. Zhang, H. Liu, X. Shi, L. Chen and G. J. Snyder, *Adv. Mater.*, 2014, **26**, 3974.

13. J.-B. Vaney, J. Carreaud, G. Delaizir, A. Pradel, A. Piarristeguy, C. Morin, E. Alleno, J. Monnier, A. P. Gonçalves, C. Candolfi, A. Dauscher and B. Lenoir, *Adv. Electron. Mater.*, 2015, DOI: 10.1002/aelm.201400008.

14. M. Christensen, S. Johnsen and B. B. Iversen, *Dalton Trans.*, 2010, **39**, 978.

15. G. S. Nolas, G. A. Slack and S. B. Schujman, in *Semiconductors and Semimetals*, edited by T. M. Tritt, Vol. 69 (Academic Press, San Diego, CA, 2001), p. 255.

16. U. Aydemir, C. Candolfi, A. Ormeci, Y. Oztan, M. Baitinger, N. Oeschler, F. Steglich and Yu. Grin, *Phys. Rev. B*, 2011, **84**, 195137.

17. P. Qiu, T. Zhang, Y. Qiu, X. Shi and L. Chen, *Energy and Environ. Sci.*, 2014, **7**, 4000.

18. K. Suekuni, F. S. Kim, H. Nishiate, M. Ohta, H. I. Tanaka and T. Takabatake, *Appl. Phys. Lett.*, 2014, **105**, 132107.

19. B. J. Wuensch, *Z. Kristallogr.*, 1964, **119**, 437.

20. L. Pauling and E. W. Neuman, *Z. Kristallogr.*, 1934, **88**, 54.

21. X. Lu, D. T. Morelli, Y. Xia, F. Zhou, V. Ozolins, H. Chi, X. Zhou and C. Uher, *Adv. Energy Mater.*, 2013, **3**, 342.

22. K. Suekuni, K. Tsuruta, T. Ariga and M. Koyano, *Appl. Phys. Exp.*, 2012, **5**, 051201.

23. X. Lu and D. T. Morelli, *Phys. Chem. Chem. Phys.*, 2013, **15**, 5762.

24. K. Suekuni, K. Tsuruta, M. Kunii, H. Nishiate, E. Nishibori, S. Maki, M. Ohta, A. Yamamoto, M. Koyano, *J. Appl. Phys.*, 2013, **113**, 043712.

25. J. Heo, G. Laurita, S. Muir, M. A. Subramanian and D. A. Keszler, *Chem. Mater.*, 2014, **26**, 2047.

26. R. Chetty, Prem Kumar D. S., G. Rogl, P. Rogl, E. Bauer, H. Michor, S. Suwas, S. Puchegger, G. Giester, R. C. Mallik, *Phys. Chem. Chem. Phys.*, 2015, **17**, 1716.

27. X. Lu and D. T. Morelli, *J. Elec. Mater.*, 2014, **43**, 1983.

28. T. Barbier, P. Lemoine, S. Gascoin, O. I. Lebedev, A. Kaltzoglou, P. Vaqueiro, A. V. Powell, R. I. Smith and E. Guilmeau, *J. Alloys Compd.*, 2015, **634**, 253.

29. Y. Bouyrie, C. Candolfi, S. Pailhès, M. M. Koza, B. Malaman, A. Dauscher, J. Tobola, O. Boisron, L. Saviot and B. Lenoir, *Phys. Chem. Chem. Phys.* DOI: 10.1039/c5cp02900g (2015).

30. E. Lara-Curzio, A. F. May, O. Delaire, M. A. McGuire, X. Lu, C.-Y. Liu, E. D. Case and D. T. Morelli, *J. Appl. Phys.*, 2014, **115**, 193515.

31. W. Lai, Y. Wang, D. T. Morelli and X. Lu, *Adv. Funct. Mater.*, 2015, **25**, 3648.

32. J. Rodriguez-Carvajal, *Physica B*, 1993, **192**, 55.

33. G. M. Sheldrick, *Acta Cryst.*, 2008, **A64**, 112.

34. A. Bansil, S. Kaprzyk, P. E. Mijnarends and J. Tobola, *Phys. Rev. B*, 1999, **60**, 13396.

35. T. Stopa, S. Kaprzyk and J. Tobola, *J. Phys.: Condens. Matter*, 2004, **16**, 4921.

36. J. P. Perdew and Y. Wang, *Phys. Rev. B*, 1992, **45**, 13244.

37. A. Pfitzner, M. Evain and V. Petricek, *Acta Cryst.*, 1997, **B53**, 337.

38. S. Kaprzyk and A. Bansil, *Phys. Rev. B*, 1990, **42**, 7358.

39. E. Alleno, D. Bérardan, C. Byl, C. Candolfi, R. Daou, R. Decourt, E. Guilmeau, S. Hébert, J. Hejtmanek, B. Lenoir, P. Masschelein, V. Ohorodniichuk, M. Pollet, S. Populoh, D. Ravot, O. Rouleau and M. Soulier, *Rev. Sci. Instrum.*, 2015, **86**, 011301.

40. A. G. Trudu and U. Knittel, *Can. Mineral.*, 1998, **36**, 1115.

41. B. J. Skinner, F. D. Luce and E. Makovicky, *Econ. Geol.*, 1972, **67**, 924.

42. E. Makovicky and B. J. Skinner, *Can. Mineral.*, 1978, **16**, 611.

43. K. Tatsuka and N. Morimoto, *Am. Mineral.*, 1973, **58**, 425.

44. K. Tatsuka and N. Morimoto, *Econ. Geol.*, 1977, **72**, 258.

45. M. L. Johnson and R. Jeanloz, *Amer. Mineral.*, 1983, **68**, 220.

46. X. Lu, D. T. Morelli, Y. Xia and V. Ozolins, *Chem. Mater.*, 2015, **27**, 408.

47. D. G. Cahill, S. K. Watson and R. O. Pohl, *Phys. Rev. B*, 1992, **46**, 6131.

48. X. Fan, E. D. Case, X. Lu and D. T. Morelli, *J. Mater. Sci.*, 2013, **48**, 7540.

Tables

Table 1. Nominal and actual compositions determined on the series S1 and S2 of polycrystalline $Cu_{12}Sb_{4-x}Te_xS_{13}$ tetrahedrites. The chemical formulae were normalized to 13 sulphur atoms per formula unit.

Series S1		*Series S2*	
Nominal composition	*Actual composition*	*Nominal composition*	*Actual composition*
$Cu_{12}Sb_3Te_1S_{13}$	$Cu_{12.24}Sb_{3.78}Te_{0.61}S_{13}$	$Cu_{12}Sb_{3.5}Te_{0.5}S_{13}$	$Cu_{12.37}Sb_{3.50}Te_{0.52}S_{13}$
$Cu_{12}Sb_{2.75}Te_{1.25}S_{13}$	$Cu_{12.44}Sb_{3.73}Te_{0.80}S_{13}$	$Cu_{12}Sb_3Te_1S_{13}$	$Cu_{12.39}Sb_{3.16}Te_{1.01}S_{13}$
$Cu_{12}Sb_{2.5}Te_{1.5}S_{13}$	$Cu_{12.51}Sb_{2.82}Te_{1.40}S_{13}$	$Cu_{12}Sb_{2.5}Te_{1.5}S_{13}$	$Cu_{12.41}Sb_{2.73}Te_{1.41}S_{13}$
$Cu_{12}Sb_{2.25}Te_{1.75}S_{13}$	$Cu_{11.98}Sb_{1.96}Te_{1.81}S_{13}$	$Cu_{12}Sb_{2.25}Te_{1.75}S_{13}$	$Cu_{11.97}Sb_{2.40}Te_{1.85}S_{13}$
$Cu_{12}Sb_2Te_2S_{13}$	$Cu_{11.99}Sb_{2.33}Te_{1.79}S_{13}$	/	/

Figure Captions

Figure 1: Perspective view of the crystal structure of $Cu_{12}Sb_4S_{13}$.

Figure 2: Chemical environment of the Cu1 (a), Cu2 (b), S1 (c), S2 (d) and Sb/Te (e) atoms in the tetrahedrite structure inferred from single-crystal x-ray diffraction.

Figure 3: Rietveld refinements of the PXRD patterns of the (a) $x = 0.52$ (series S2) and (b) $x = 1.79$ samples (series S1). The experimental data are marked as red dots, the calculated pattern is in black and the difference between experimental and calculated patterns is shown in blue. The vertical green bars stand for the expected Bragg positions of the cubic crystal lattice of tetrahedrites.

Figure 4: Lattice parameter a as a function of the actual Te content x of the series S1 (a) and S2 (b). In both panels, the value of a of the ternary composition obtained by Pfitzner *et al*. (Ref. 37) in a single-crystalline specimen is indicated by the filled square blue symbol. (c) Temperature dependence of the lattice parameter a of the $x = 0.61$ (red filled circle: heating; blue filled square: cooling) and $x = 1.79$ (green filled triangle: heating) tetrahedrites.

Figure 5: DSC traces for the $x = 1.79$ (a), $x = 0.61$ (b) (series S1) and the $x = 1.01$ (c) samples.

Figure 6: Dispersion curves along high symmetry directions in the Brillouin zone for $x = 0.0$ and $x = 2.0$. The Fermi level has been arbitrarily set to 0 eV.

Figure 7: Total and partial densities of states of the $x = 0.0$ and $x = 2.0$ compounds.

Figure 8: Temperature dependence of the electrical resistivity ρ of $Cu_{12}Sb_{4-x}Te_xS_{13}$ tetrahedrites for $x = 0.61$, 0.80, 1.40, 1.81 and 1.79 (series S1, panel a) and for $x = 0.52$, 1.01, 1.41 and 1.85 (series S2, panel b).

Figure 9: Thermopower α as a function of temperature for the series S1 ($x = 0.61$, 0.80, 1.40, 1.81 and 1.79, panel a) and S2 ($x = 0.52$, 1.01, 1.41 and 1.85, panel b).

Figure 10: Total thermal conductivity κ as a function of temperature in the series S1 (a) and S2 (b). The color-coded symbols used in panel b) and c) are identical. (c) Temperature dependence of the lattice thermal conductivity κ_L of the samples of the series S2.

Figure 11: Temperature dependence of the dimensionless figure of merit ZT for $Cu_{12}Sb_{4-x}Te_xS_{13}$ for $x = 0.61$, 0.80, 1.40, 1.81 and 1.79, (series S1, panel a) and for $x = 0.52$, 1.01, 1.41 and 1.85, (series S2, panel b).

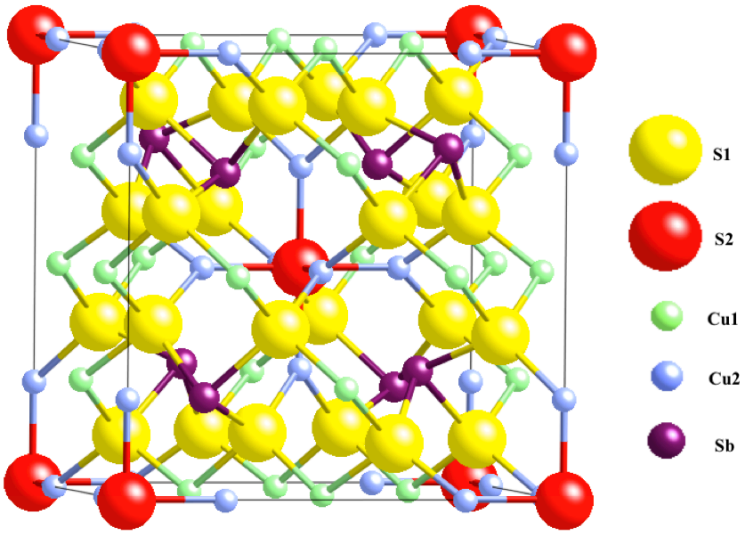

Figure 1

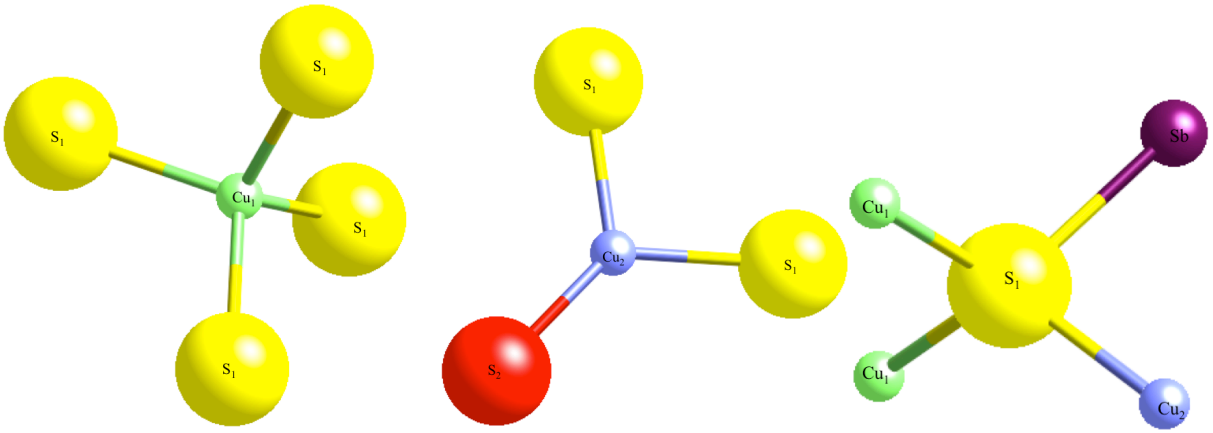

(a) (b) (c)

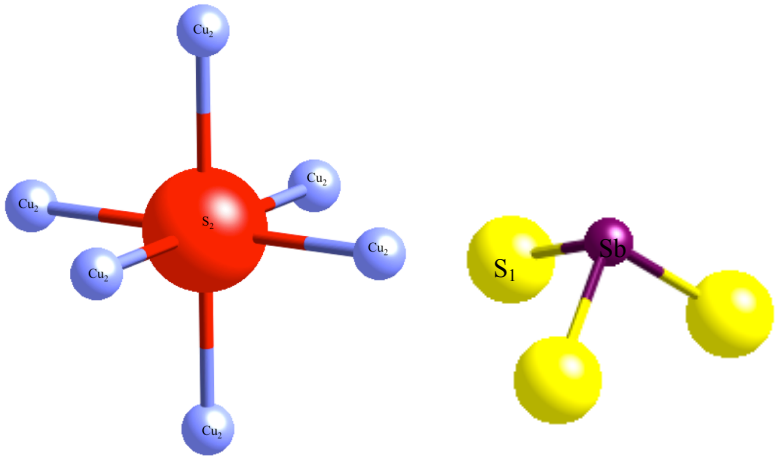

(d) (e)

Figure 2

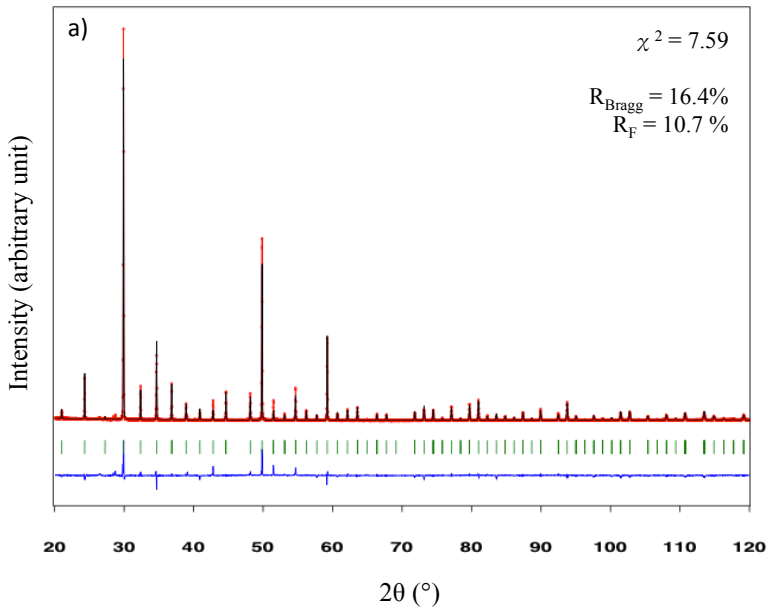
a)
$\chi^2 = 7.59$
$R_{Bragg} = 16.4\%$
$R_F = 10.7\ \%$
Intensity (arbitrary unit)
20 30 40 50 60 70 80 90 100 110 120
2θ (°)

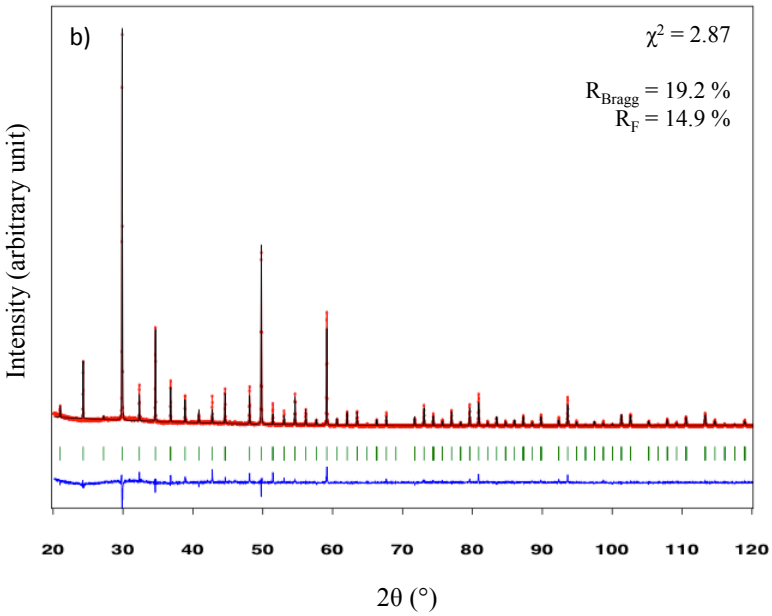
b)
$\chi^2 = 2.87$
$R_{Bragg} = 19.2\ \%$
$R_F = 14.9\ \%$
Intensity (arbitrary unit)
20 30 40 50 60 70 80 90 100 110 120
2θ (°)

Figure 3

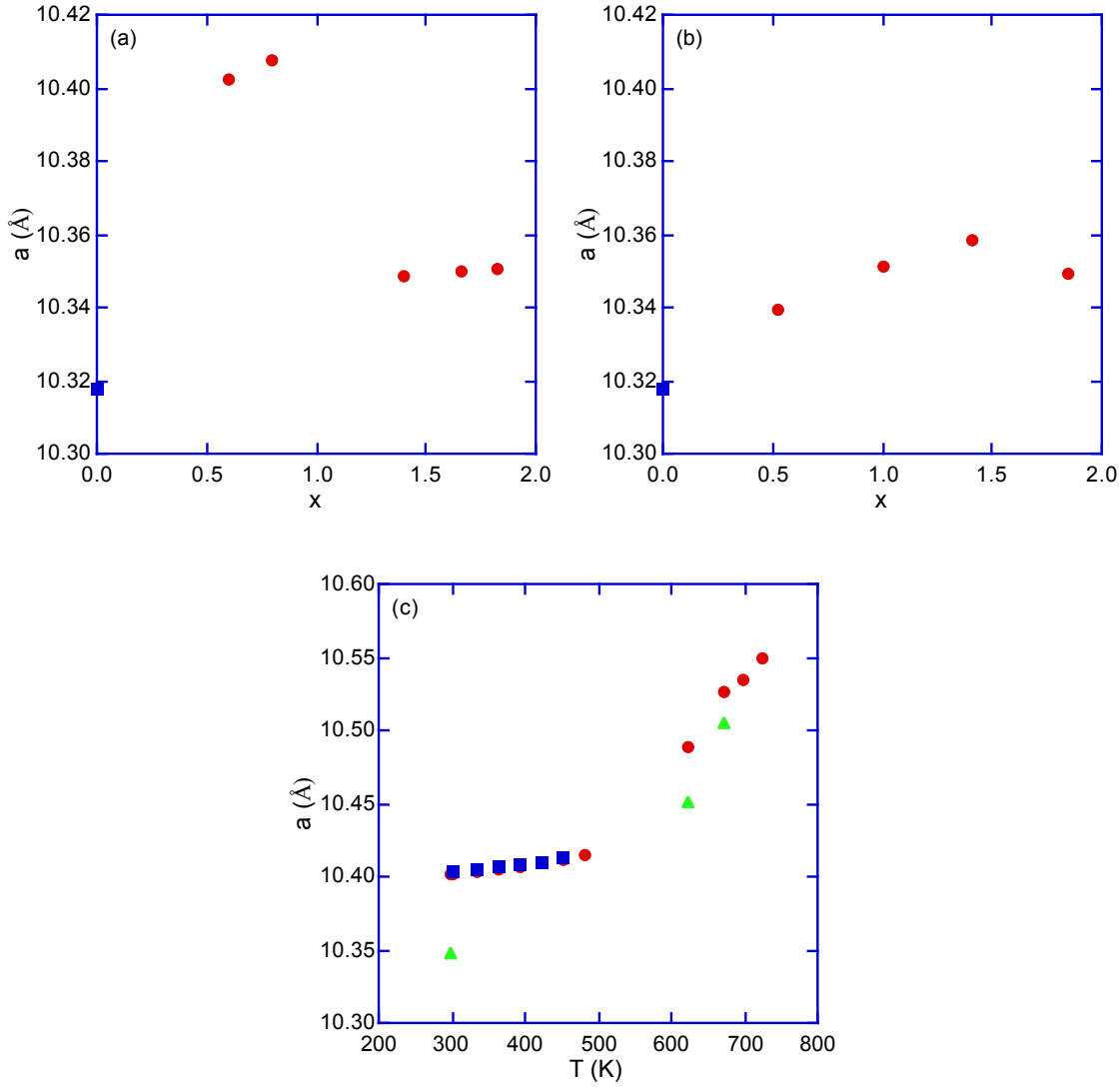
(a)
(b)
(c)
a (Å)
x
T (K)
10.42
10.40
10.38
10.36
10.34
10.32
10.30
0.0
0.5
1.0
1.5
2.0
10.60
10.55
10.50
10.45
10.40
10.35
200
300
400
500
600
700
800

Figure 4

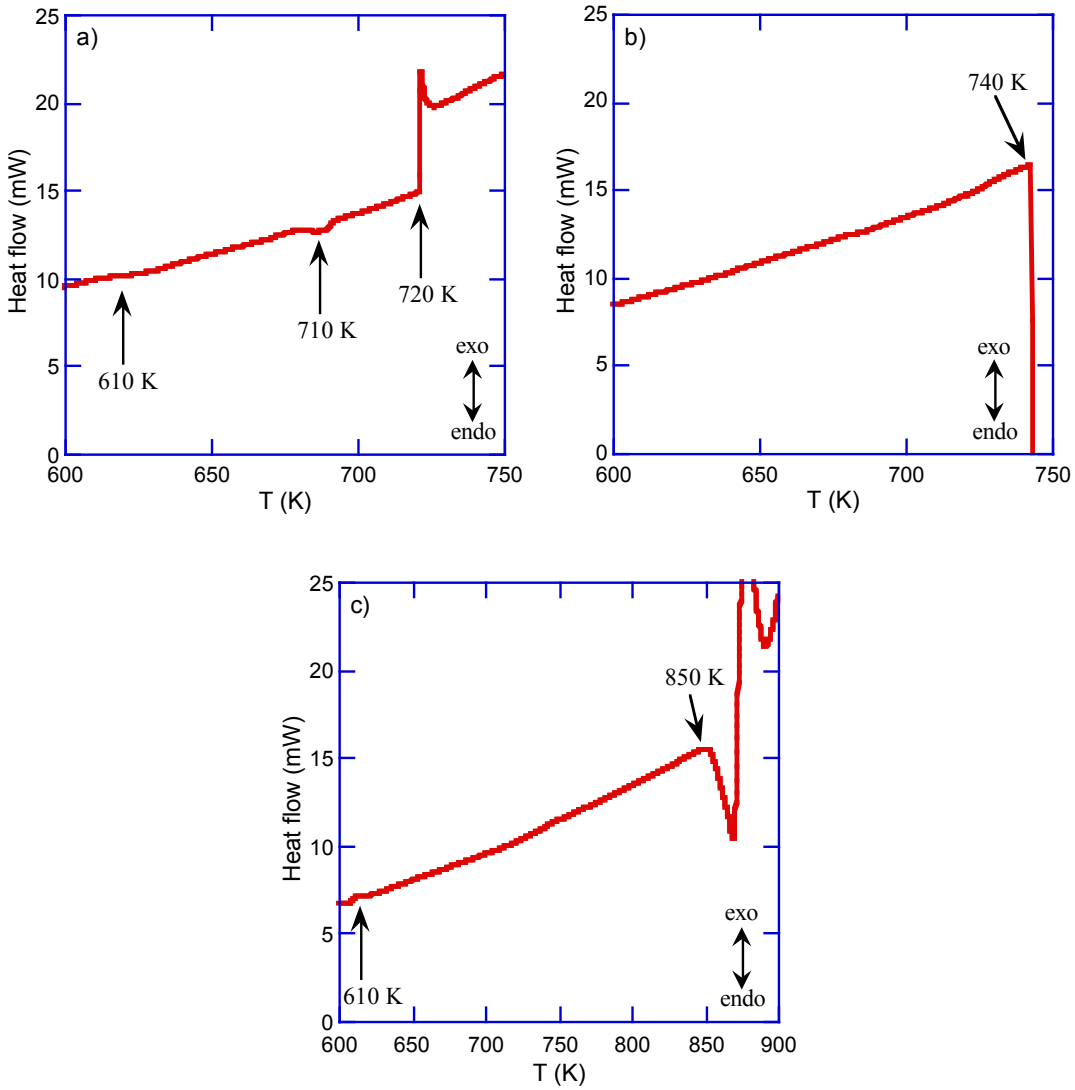

Figure 5

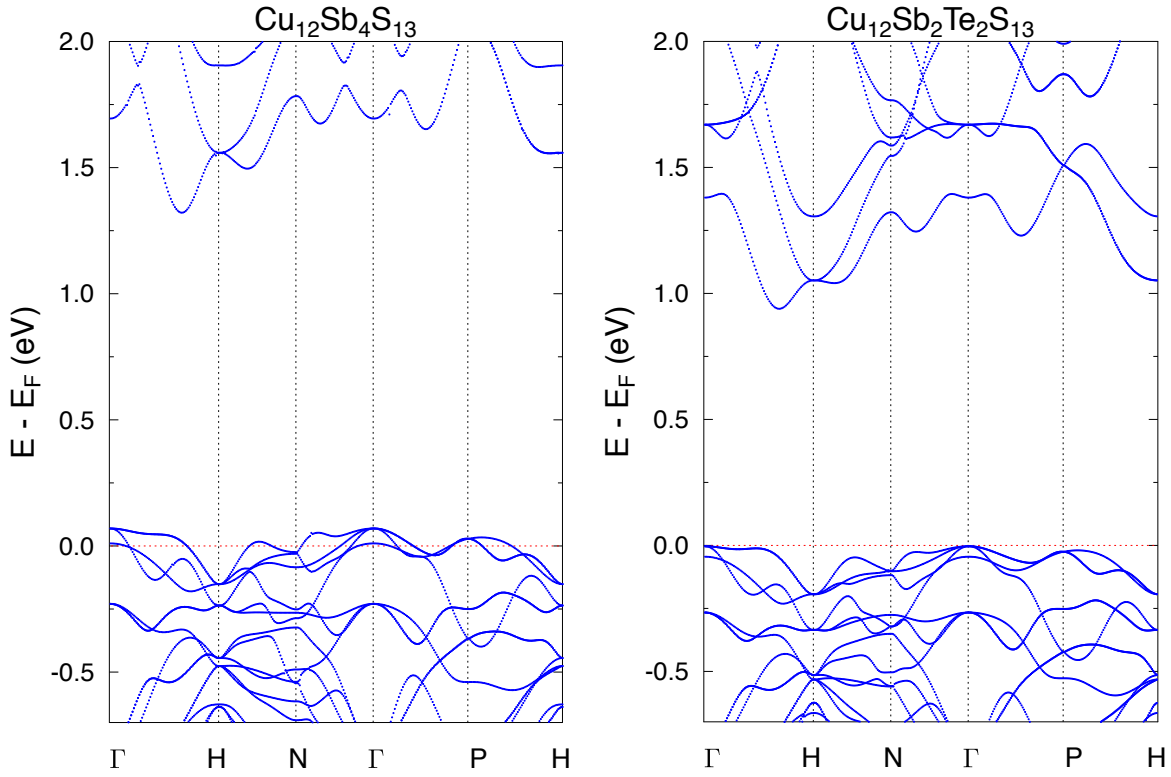

Figure 6

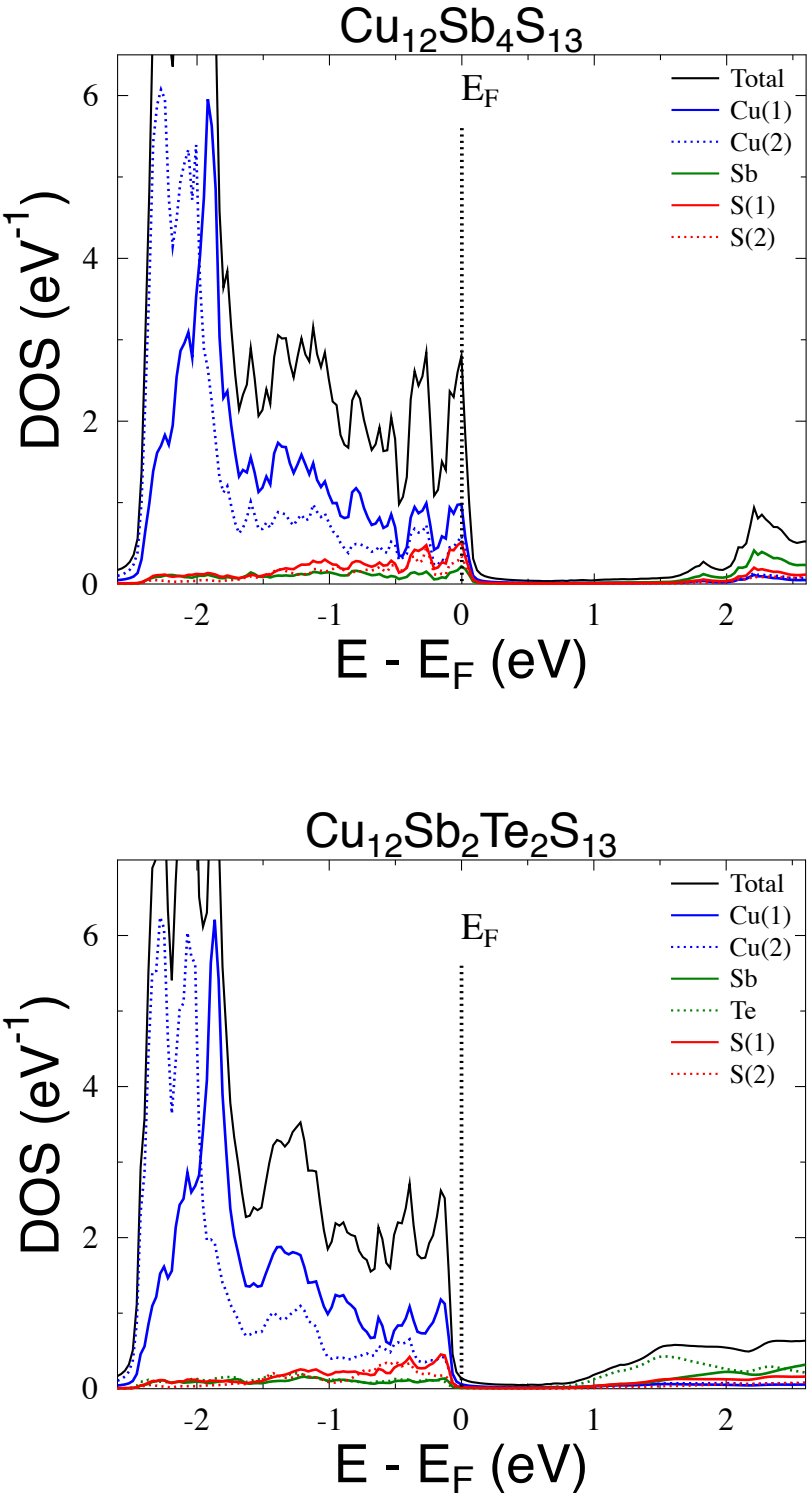
Cu12Sb4S13
EF
Total
Cu(1)
Cu(2)
Sb
S(1)
S(2)
DOS (eV-1)
E - EF (eV)
Cu12Sb2Te2S13
EF
Total
Cu(1)
Cu(2)
Sb
Te
S(1)
S(2)
DOS (eV-1)
E - EF (eV)

Figure 7

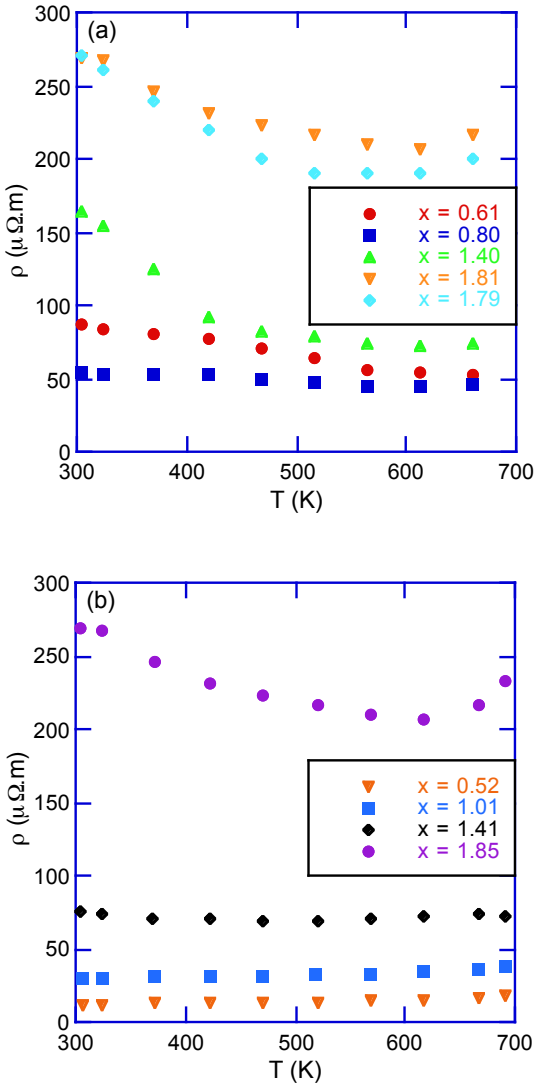
(a)
ρ (μΩ.m)
T (K)
x = 0.61
x = 0.80
x = 1.40
x = 1.81
x = 1.79
(b)
ρ (μΩ.m)
T (K)
x = 0.52
x = 1.01
x = 1.41
x = 1.85

Figure 8

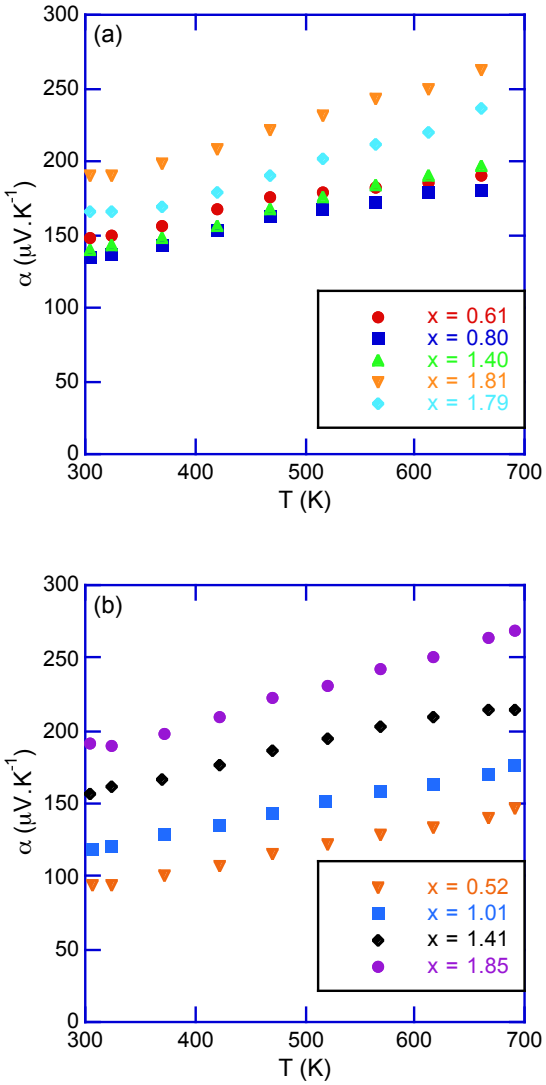
(a)
α (μV.K-1)
T (K)
x = 0.61
x = 0.80
x = 1.40
x = 1.81
x = 1.79
(b)
α (μV.K-1)
T (K)
x = 0.52
x = 1.01
x = 1.41
x = 1.85

Figure 9

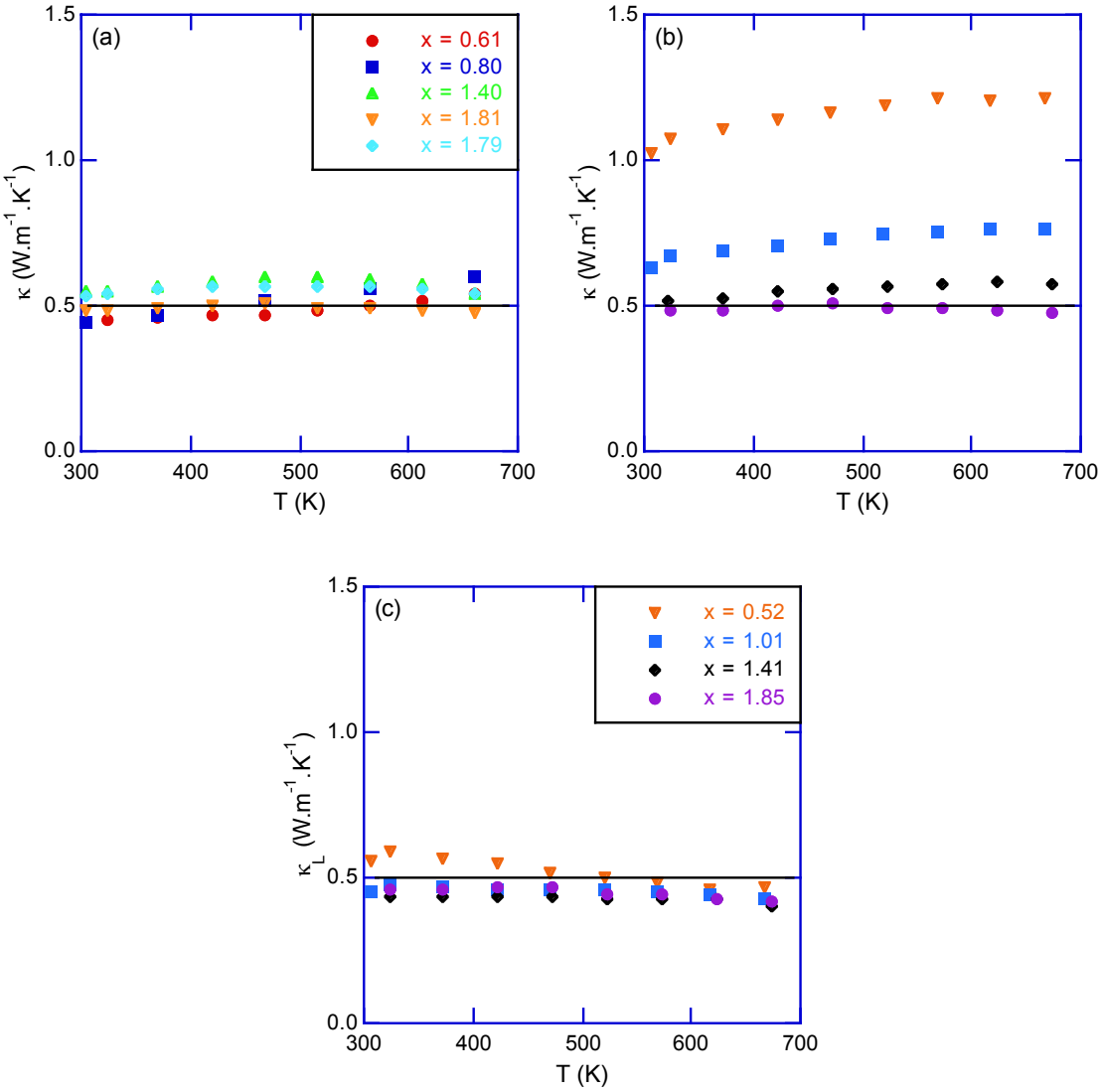
(a)
x = 0.61
x = 0.80
x = 1.40
x = 1.81
x = 1.79
κ (W.m-1.K-1)
T (K)
(b)
(c)
x = 0.52
x = 1.01
x = 1.41
x = 1.85
κL (W.m-1.K-1)

Figure 10

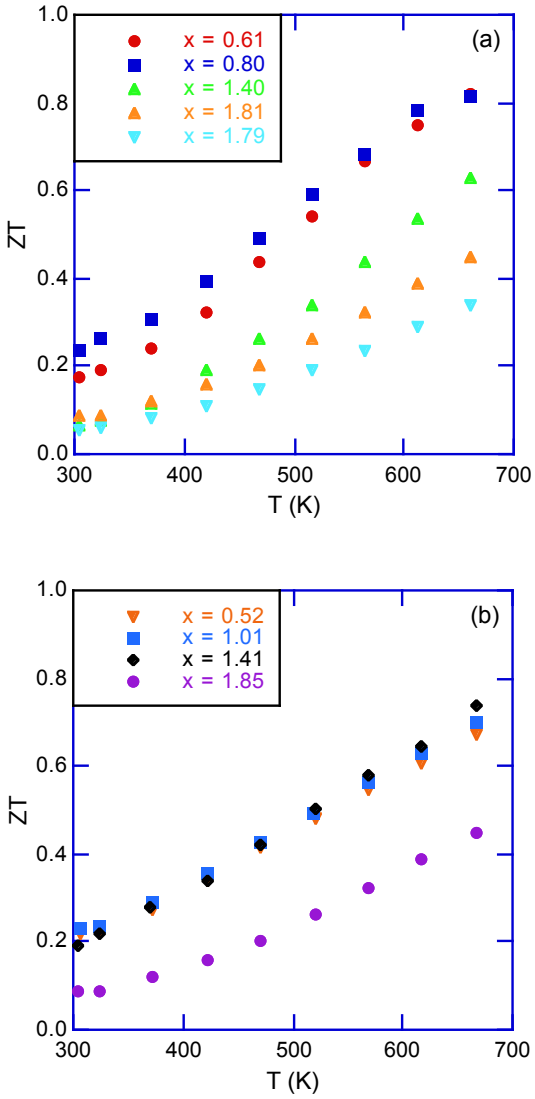
(a)
x = 0.61
x = 0.80
x = 1.40
x = 1.81
x = 1.79
ZT
T (K)
1.0
0.8
0.6
0.4
0.2
0.0
300
400
500
600
700
(b)
x = 0.52
x = 1.01
x = 1.41
x = 1.85
ZT
T (K)

Figure 11